

Optics Letters

Wide-field interferometric measurement of a nonstationary complex coherence function

ROXANA REZVANI NARAGHI,¹ HEATH GEMAR,¹ MAHED BATARSEH,¹ ANDRE BECKUS,² GEORGE ATIA,² SERGEY SUKHOV,¹ AND ARISTIDE DOGARIU^{1,*}

¹CREOL, The College of Optics and Photonics, University of Central Florida, 4000 Central Florida Blvd., Orlando, Florida 32816, USA

²Department of Electrical and Computer Engineering, University of Central Florida, 4000 Central Florida Blvd., Orlando, Florida 32816, USA

*Corresponding author: adogariu@creol.ucf.edu

Received 30 August 2017; accepted 26 October 2017; posted 3 November 2017 (Doc. ID 305765); published 27 November 2017

Spatial coherence function (SCF) is a complex function of two spatial coordinates that, in general, carries more information than the bare intensity distribution. A fast and quantitatively accurate measurement of the SCF is extremely important for a range of applications in optical sensing and imaging. Here, we demonstrate an efficient two-step procedure for measuring the full-field complex coherence function. The measurement relies on an optimized design of a wavefront shearing interferometer capable of characterizing spatially inhomogeneous fields over an extended angular domain. The measurement precision is confirmed by the excellent agreement with a numerical estimation based on Fresnel calculations. We demonstrate that the sensitivity and the measurement range afforded by our instrument permits us to reliably describe the differences in the complex coherence functions that are due to subtle modifications in the shape, position, and orientation of radiation sources. © 2017 Optical Society of America

OCIS codes: (030.1640) Coherence; (120.3180) Interferometry; (120.4820) Optical systems.

<https://doi.org/10.1364/OL.42.004929>

Comprehensive characterization of optical fields involves determining the complex field-field correlations. The spatial coherence function (SCF) of an electromagnetic field can be measured using interferometric or non-interferometric methods. Phase-space non-interferometric measurements require a resolution trade-off between the spatial and angular sampling [1,2]. Interferometric techniques directly access the field correlation functions and can be implemented based on either wavefront sampling or wavefront shearing approaches. The wavefront sampling approach relies on the classical setting of Young's two pinholes starting from Zernike's suggestion [3] and the pioneering experiments of Thompson and Wolf [4]. Since then, a variety of techniques have been developed to improve the measurement performance and to decrease the experiment time, including the number of redundant [5] or

non-redundant arrays of pinholes [6], multiple aperture masks [7], pairs of non-parallel slits [8], reversed wavefront interferometry [9], and programmable apertures [10,11]. The alternative technique, wavefront shearing, can be implemented in interferometric settings such as the common path Sagnac [12,13] or grating shear interferometers [14]. All these approaches have their own specific limitations in terms of light throughput, system complexity, duration, and precision of the measurement.

Here, we demonstrate a compact and fully automated instrument capable of accurate measurements of complex coherence functions along any desired direction and with widths varying over more than two orders of magnitude. The measurement is based on a wavefront shearing interferometer in which the real and imaginary parts of the SCF are obtained over a large field of view using only two measurements. The system's accuracy and the operation capabilities will be demonstrated in coherence measurements of broad-bandwidth radiation emitted from a variety of shaped, equal-area sources.

To measure the complex SCF of inhomogeneous and highly divergent fields, the instrument should have a large field of view. Shear interferometers based on repositioning refractive optical elements such as lenses or glass blocks are rather limited because of the inherent astigmatism [12,15,16]. Translating reflective elements on the other hand affords a larger field of view [13]. We used this approach and integrated a telescopic imaging system with a Sagnac interferometer, as illustrated in Fig. 1.

Of course, the field of view can be enlarged by using larger optical elements, but it can also be increased by reducing the interferometer length d (the path length between lenses L2 and L3 in Fig. 1). However, it should be noted that there is always a trade-off between the field of view and spherical aberrations. More specifically, in order to decrease d , lens L2 with a smaller focal length is needed. This leads to a larger radius of curvature which, in turn, causes spherical aberrations in the system. To address this issue, we designed the Dual-Phase Sagnac Interferometer (DuPSal) in such a way to optimize the field of view and minimize the spherical aberrations. To maximize the amount of light passing through the system while avoiding vignetting, the lens L1 (focal length 9 mm, iris diameter 2 mm)

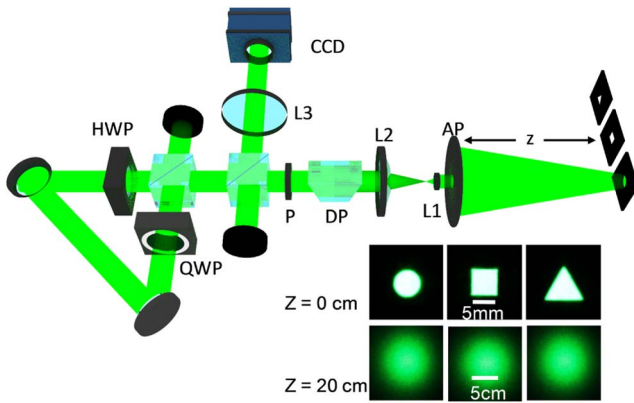


Fig. 1. Schematic of the experimental setup for measuring the SCF at the plane of the input AP. The source is a green LED with a 30 nm bandwidth centered at of 525 nm and placed at $z = 1$ m from AP. L1, L2, L3, lenses; HWP, half-wave plate; QWP, quarter-wave plate; DP, Dove prism; P, polarizer. The inset shows the intensity distributions of differently shaped sources recorded in the source plane (top row) and at 20 cm distance (bottom row).

images the input aperture (AP) on the plane of Lens L2 (focal length 100 mm, diameter 10 mm). The lens L2 creates an image of L1 at the plane of the lens L3 (focal length 300 mm, diameter 25.4 mm) and, finally, L3 images L2 and thus, the AP, at the camera. Based on these optical components and the alignment parameters, we estimated that the numerical AP is approximately 0.13, a value that is also confirmed by the smallest value of the measured coherence length.

A distinctive feature of our design is the rotating Dove prism placed between the telescopic imaging system and the Sagnac interferometer. In this way, our DuPSaI instrument is capable of measuring the SCF along any desired shear direction.

To create the necessary field replicas and to avoid any birefringence [17], we use a polarizer placed after the Dove prism and a non-polarizing 50/50 beam splitter that divides the incoming field into two identical copies. These copies counter-propagate along a common path that consists of two flat mirrors, a half-wave plate (HWP) and a quarter-wave plate (QWP), as shown in Fig. 1. The symmetrical lateral shear, \mathbf{s} , is introduced with respect to the original position by the simultaneous movement of the mirrors while maintaining the original path length. This is accomplished using a motorized stage (Newport MFA-PPD) in conjunction with a controller (ESP300) that ensures a movement repeatability within 0.12 μm . The phase delays between the two field replicas are introduced by rotating the HWP using a computer-controlled stage (CONEX-AGP) with a built-in feedback that provides an accuracy better than 0.08 deg. The interference patterns resulting from the interference of the two field replicas are imaged onto an EMCCD (Andor Xion 888). The entire system is automated and controlled via a LabVIEW code developed in house.

We note that the current design permits using the entire optical field impinging on the input AP, and the full coherence function can be determined without any modifications to the setup. In order to obtain both the real and the imaginary part of the SCF, we first record a series of intensity patterns for multiple shearing distances \mathbf{s} , while the fast axes of each wave plate are parallel with the direction of incident polarization:

$$I^0(\mathbf{r}, \mathbf{s}) = I\left(\mathbf{r} + \frac{\mathbf{s}}{2}\right) + I\left(\mathbf{r} - \frac{\mathbf{s}}{2}\right) + 2 \text{Re}[\Gamma(\mathbf{r}, \mathbf{s})], \quad (1)$$

where $\Gamma(\mathbf{r}, \mathbf{s}) = \langle E(\mathbf{r} + \frac{\mathbf{s}}{2})E^*(\mathbf{r} - \frac{\mathbf{s}}{2}) \rangle$ is the SCF to be measured. A π phase difference is then introduced between the two interfering waves by rotating the HWP plate by $\pi/4$ radians, and a second series of intensities is recorded to obtain

$$I^{\pi/4}(\mathbf{r}, \mathbf{s}) = I\left(\mathbf{r} + \frac{\mathbf{s}}{2}\right) + I\left(\mathbf{r} - \frac{\mathbf{s}}{2}\right) + 2 \text{Im}[\Gamma(\mathbf{r}, \mathbf{s})]. \quad (2)$$

Conventional shearing interferometry would require two more measurements using an additional waveplate to retrieve the complex SCF, which makes the procedure unnecessarily complicated [12]. In our approach, one takes advantage of some properties of a common path interferometer to accomplish this task with only two orientations of the wave plate, i.e., two relative phases (hence, the name of our system). At zero shear, $\text{Re}[\Gamma(\mathbf{r}, 0)] = I(\mathbf{r})$ and, therefore, $I^0(\mathbf{r}, 0) = 4 \cdot I(\mathbf{r})$, which allows recovering the real and imaginary components of the SCF as

$$\text{Re}[\Gamma(\mathbf{r}, \mathbf{s})] = 0.5(I^0(\mathbf{r}, \mathbf{s}) - 0.5I^0(\mathbf{r}, 0)),$$

$$\text{Im}[\Gamma(\mathbf{r}, \mathbf{s})] = 0.5(I^{\pi/4}(\mathbf{r}, \mathbf{s}) - 0.5I^0(\mathbf{r}, 0)). \quad (3)$$

To establish the sensitivity of DuPSaI measurements, we first examined the SCF of the optical fields radiated from two circular APs, 6 and 5.5 mm in diameter, which differ by only 9% in size. In the experiment, the APs were illuminated by a high-power LED with a peak wavelength of 525 nm and a bandwidth of 30 nm (Thorlabs, Solis-525C) and were placed at 1 m distance from the input AP of the DuPSaI. Using the procedure outlined above, we were able to measure both the magnitude and the phase of the SCF over a wavefront extent of 4 mm around the optical axis. The results are summarized in Fig. 2, where we plot the complex degree of coherence (CDC), $\gamma(\mathbf{r}, \mathbf{s}) = \Gamma(\mathbf{r}, \mathbf{s}) / \sqrt{I(\mathbf{r} + \frac{\mathbf{s}}{2})I(\mathbf{r} - \frac{\mathbf{s}}{2})}$ corresponding to different sources of radiation. The difference between the coherence properties of radiation emitted by sources with diameters of 6 and 5.5 mm is clearly visible.

To further confirm the accuracy of our measurement, we compared the experimental results with numerical estimates. We assumed monochromatic radiation emitted by a Gaussian-correlated light source with the SCF of the form

$$\Gamma_s(x, y, s_x, s_y) = I_{\text{in}}(x, y) \exp\left(-\frac{s_x^2}{2\sigma^2}\right) \exp\left(-\frac{s_y^2}{2\sigma^2}\right), \quad (4)$$

where the uniform intensity distribution $I_{\text{in}}(x, y)$ describes the corresponding shape of the mask, and σ is the standard deviation of the Gaussian-correlated source with the extent of spatial coherence of $l_c = 4.1 \mu\text{m}$ in the plane of the source (full width at half-maximum).

The SCF of the field in the plane of the input AP was calculated using the corresponding Fresnel integrals [18]

$$\begin{aligned} \Gamma(x, y, s_x, s_y; z) &= \frac{1}{(\lambda z)^2} \iint \iint dx' dy' ds'_x ds'_y \\ &\times H(x, x', s_x, s'_x; z) H(y, y', s_y, s'_y; z) \\ &\times \Gamma_s(x', y', s'_x, s'_y), \end{aligned} \quad (5)$$

where z is the total propagation distance from the source to the detector, λ is the wavelength, $k = \frac{2\pi}{\lambda}$ is the wavenumber, and

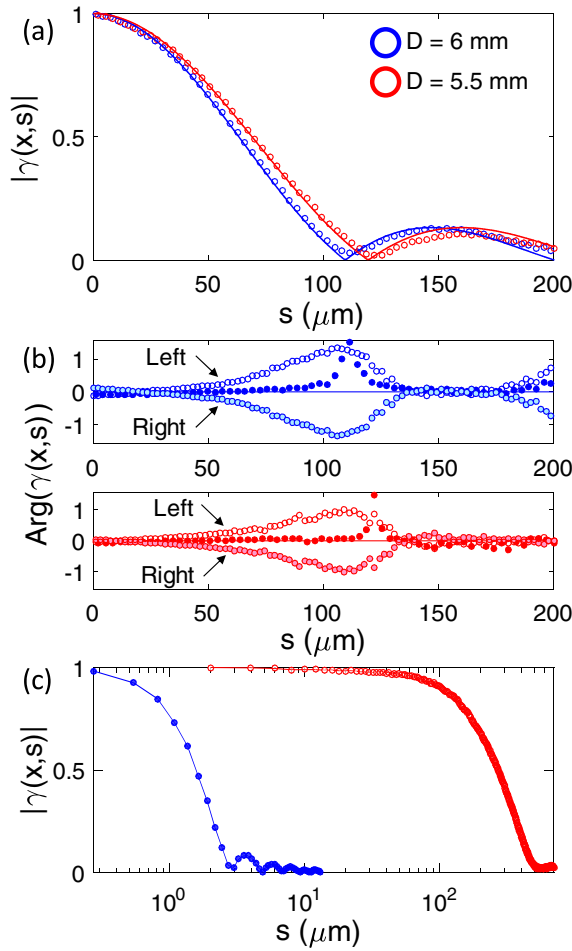


Fig. 2. (a) Measured magnitude of CDC corresponding to different source diameter sizes (hollow circles), together with corresponding full Fresnel integral calculations (solid lines). (b) Corresponding CDC phases measured along the optical axis and 200 μm to the left and right of the optical axis. (c) Extended range of measurable CDC: the blue circles denote the CDC magnitude right after a 50.8 mm partially coherent source, while the red circles represent the same quantity after 210 cm free-space propagation away from a partially coherent source of 3 mm in diameter.

$H(x, x', s, s'; z) = \exp\left[\frac{ik}{z}(x + x')(s - s')\right]$ is the free-space Green's function. The function $\Gamma(\mathbf{r}, \mathbf{s})$ was evaluated along the same shear direction x as in the experiment, and the results are plotted with solid lines in Figs. 2–4. The agreement between the measurements and these numerical estimations is remarkable. For instance, for the coherence functions in Fig. 2(a), the Pearson correlation coefficient takes values of 0.97 and 0.96 for the 6 and 5.5 mm APs, respectively.

DuPSaI also demonstrates the ability to measure the SCF within a wide range of coherence lengths. In Fig. 2(c), we show two extreme cases with $l_c = 3.2$ μm and $l_c = 540$ μm measured right next to the 50.8 mm diameter partially coherent source and after 2.1 m free-space propagation of light away from a 3 mm diameter partially coherent source, correspondingly. We emphasize that this range is covered without any modification or adjustment to the DuPSaI system.

Another important feature of DuPSaI, common to wave-front shearing approaches, is the extended field of view, which

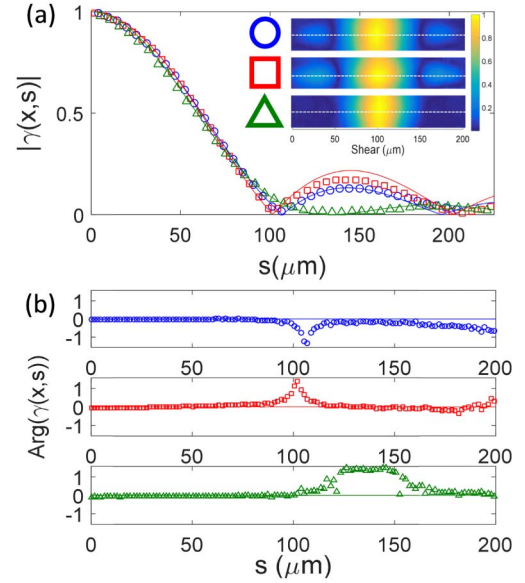


Fig. 3. (a) Measured magnitude of CDC corresponding to different source shapes (marker lines), together with corresponding calculations using the Fresnel integral (solid lines). The inset is the experimental 2D coherence function, while the white dotted lines indicate the cross-sectional part plot in (a). (b) Corresponding CDC phases.

allows measuring the nonstationary (spatially varying) SCF. In our case, the non-stationarity manifested in a phase variation across the image that served as an indicator of the source location. These results are illustrated in Fig. 2(b), where we plot the phases corresponding to the measurements performed along the optical axis, together with measurements at 200 μm to the right and left of the optical axis.

In the following, we illustrate the DuPSaI's ability to discriminate between sources that differ only in their shapes. For this purpose, we constructed three different APs having different shapes (circle, square, and equilateral triangle), but the same area of 2.83×10^{-5} m^2 to emulate sources emitting the same amount of power within the same spectral range. As can be seen in the inset of Fig. 1, the shape information is already lost in the intensity distribution recorded at 20 cm away from the source. However, quite different coherence functions are being detected at 100 cm from the source, as seen in Fig. 3.

When compared with the Fresnel estimations, a good agreement is found for all shapes. We note that, even though the sources have the same area, the length of the average chord (\bar{x} parallel to the direction of shear) are different: 5.32 mm for the square, 4.76 mm for the disk, and 4.04 mm for the triangular source. These values are inversely proportional to the location of the first SCF minimum, as evident from the results summarized in Fig. 3. Note that, the second peak of the coherence function for the equilateral triangle drops significantly. This is due to the large variation of the chord length in the shear direction. More specifically, in the paraxial approximation for a delta-correlated source, the complex coherence function is essentially the Fourier transform of the source shape. Thus, variations of the source size across the shearing direction alter the first minimum and the amplitude of the second peak [19,20].

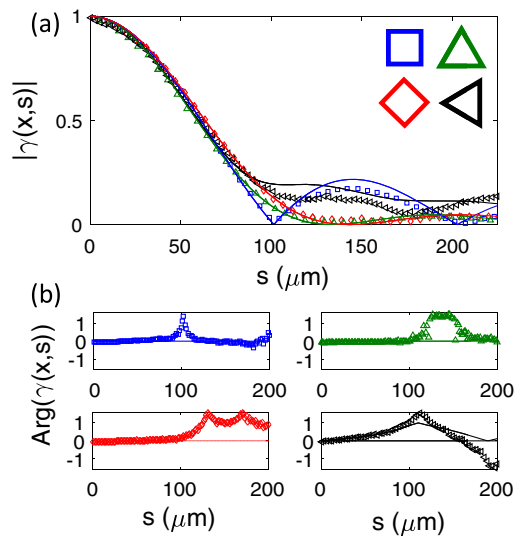


Fig. 4. (a) Measured magnitude of CDC corresponding to different source shapes, as well as different orientations of the source, together with corresponding simulations using the full Fresnel integral. (b) Corresponding CDC phases.

Finally, we will show how DuPSaI measurements can be used to discriminate between different orientations of the source. In Fig. 4, we present the experimental results corresponding to the square AP rotated by 45 deg and the equilateral triangle rotated by 90 deg. By rotating the square AP by 45 deg, the chord length is no longer constant, and the average chord length becomes 3.76 mm. Consequently, the first minimum shifts to larger values, and the second peak drops significantly. The case of the equilateral triangle, on the other hand, will be left-right asymmetric after 90 deg rotation around its center. The asymmetric shape of the source imposes a non-zero phase as can be seen from Fig. 4(b).

In conclusion, we have developed a compact and fully automated interferometric instrument capable of measuring a wide range of complex coherence functions. The instrument composes a Sagnac interferometer integrated with a telescopic imaging system and permits determining the complex SCF from only two measurements. The coherence functions can be determined along any desired direction and over more than two orders of magnitude of spatial extent.

The sensitivity, accuracy, and extended measurement range were quantitatively assessed. In particular, we have shown that by reliable coherence measurements one can discriminate between sizes, shapes, and orientations of radiation sources in

conditions where the intensity distributions contain no useful information. The results of our experiments were compared to rigorous estimations based on Fresnel integrals. We have found excellent agreement (Pearson correlation better than 0.96) for both the amplitude and the phase of the SCFs.

Moreover, the experimental design allows for wide-field coherence measurements, which permits detecting spatially nonstationary properties of the field. Therefore, we were able to demonstrate the system's ability to locate the center of mass of the source of radiation within the extended field of view. The unique capabilities of this instrument should be of interest for a range of applications in remote sensing.

Here, we have demonstrated high-resolution measurements of scalar coherence functions. Access to other elements of the full-field correlation matrix could be available by adding additional polarimetric features to the Sagnac interferometer [21].

Funding. Defense Advanced Research Projects Agency (DARPA) (HR0011-16-C-0029)

REFERENCES

1. E. Baleine and A. Dogariu, J. Opt. Soc. Am. A **20**, 2041 (2003).
2. S. Cho, M. A. Alonso, and T. G. Brown, Opt. Lett. **37**, 2724 (2012).
3. F. Zernike, Physica **5**, 785 (1938).
4. B. J. Thompson and E. Wolf, J. Opt. Soc. Am. **47**, 895 (1957).
5. J. J. A. Lin, D. Paterson, A. G. Peele, P. J. McMahon, C. T. Chantler, K. A. Nugent, B. Lai, N. Moldovan, Z. Cai, D. C. Mancini, and I. McNulty, Phys. Rev. Lett. **90**, 074801 (2003).
6. Y. Mejía and A. I. González, Opt. Commun. **273**, 428 (2007).
7. P. Petrucci, R. Riesenberger, U. Hübner, and R. Kowarschik, Opt. Commun. **285**, 389 (2012).
8. S. Divitt, Z. J. Lapin, and L. Novotny, Opt. Express **22**, 8277 (2014).
9. M. Santarsiero and R. Borghi, Opt. Lett. **31**, 861 (2006).
10. J.-M. Choi and J. Korean, Phys. Soc. **60**, 177 (2012).
11. H. E. Kondakci, A. Beckus, A. E. Halawany, N. Mohammadian, G. K. Atia, and A. F. Abouraddy, Opt. Express **25**, 13087 (2017).
12. C. Iaconis and I. A. Walmsley, Opt. Lett. **21**, 1783 (1996).
13. C.-C. Cheng, M. G. Raymer, and H. Heier, J. Mod. Opt. **47**, 1237 (2000).
14. J. Schwider, Appl. Opt. **23**, 4403 (1984).
15. M. V. R. K. Murty, Appl. Opt. **3**, 853 (1964).
16. D. Naik, T. Ezawa, R. Singh, Y. Miyamoto, and M. Takeda, Opt. Express **20**, 19658 (2012).
17. M. Ivan, I. Moreno, G. Paez, and M. Strojnik, Opt. Commun. **220**, 257 (2003).
18. M. Born and E. Wolf, *Principles of Optics* (Elsevier, 2013).
19. D. Kohler and L. Mandel, J. Opt. Soc. Am. **63**, 126 (1973).
20. J. R. Fienup, Opt. Lett. **3**, 27 (1978).
21. M. Mujat, E. Baleine, and A. Dogariu, J. Opt. Soc. Am. A **21**, 2244 (2004).